Environmental Science Nano

ROYAL SOCIETY OF CHEMISTRY

PAPER

View Article Online
View Journal | View Issue



Cite this: *Environ. Sci.: Nano*, 2022, **9**, 1639

# One-step biosynthesis of a bilayered graphene oxide embedded bacterial nanocellulose hydrogel for versatile photothermal membrane applications†

Govindaraj Divyapriya,[ab] Asifur Rahman,[ab] Weinan Leng,[ab] Wei Wang[ab] and Peter J. Vikesland *[ab]

Received 17th August 2021,
Accepted 10th March 2022

DOI: 10.1039/d1en00754h

rsc.li/es-nano

We introduce the facile one-step biosynthesis of a bilayer structured hydrogel composite of reduced-graphene oxide (rGO) and bacterial nanocellulose (BNC) for multiple photothermal water treatment applications. One-step *in situ* biosynthesis of a bilayered hydrogel was achieved *via* modification of BNC growth medium supplemented with an optimized concentration of corn steep liquor as a growth enhancer. A two-stage, growth rate-controlled formation mechanism for the bilayer structure was revealed. The final cleaned and freeze-dried reduced-GO embedded BNC bilayer membrane enables versatile applications such as filtration (tested using gold nanoparticles, *Escherichia coli* cells, and plasmid DNA), photothermal disinfection of entrapped *E. coli*, and solar water evaporation. Comparable particle rejection (up to ≈4 nm) and water flux (146 L $h^{-1}$ $m^{-2}$) to ultrafiltration were observed. Entrapment and photothermal inactivation of *E. coli* cells were accomplished within 10 min of solar exposure (one sun). Such treatment can potentially suppress membrane biofouling. The steam generation capacity was 1.96 kg $m^{-2}$ $h^{-1}$. Our simple and scalable approach opens a new path for biosynthesis of nanostructured materials for environmental and biomedical applications.

### Environmental significance

The sustainability capacity of the developing world is being stressed by ever-increasing demands for clean water and energy resources. Efficient tapping of abundant solar energy to harvest clean water is a viable solution to this issue. Developing nano-enabled photothermal membranes is a step forward towards sustainable water purification through filtration, photothermal disinfection and distillation. The layered integration of desired functions of photothermal materials onto a suitable support material without compromising its chemical, thermal and mechanical properties remains challenging. In this study, we demonstrate a one-step green approach to biosynthesize a bilayer structured hydrogel composite of graphene oxide (GO) and bacterial nanocellulose (BNC) through modifications of the growth rate of BNC producing bacteria *Gluconacetobacter xylinus*. The *in situ* integration of GO layers onto the BNC fiber network was controlled *via* amending the corn steep liquor as a bacterial growth enhancer. The multipurpose nature of the biosynthesized photothermal membranes was explored.

## 1. Introduction

Solar driven water treatment processes are gaining tremendous attention owing to the global water crisis.[1] Photothermal water treatment processes provide opportunities to develop low cost, decentralized, modular, and integrative approaches to produce clean water in resource-limited regions.[2] Photothermal materials that efficiently absorb and convert the broad electromagnetic spectrum of incident sunlight into thermal energy can be designed and applied for targeted treatment.[1,3] Exemplary photothermal approaches include bacterial inactivation to control biofouling in reverse osmosis/ultrafiltration membranes, photothermal evaporation/distillation, and hybrid photothermal–photocatalysis processes.[2,4–7] A range of inorganic metals and metal oxides and carbon nanomaterials have been reported for their high light-to-heat conversion efficiencies.[1,3] Metal and semiconductor-based photothermal

[a] *Department of Civil and Environmental Engineering, Virginia Tech, Blacksburg, Virginia, USA. E-mail: pvikes@vt.edu*
[b] *Virginia Tech Institute of Critical Technology and Applied Science (ICTAS), Sustainable Nanotechnology Center (VTSuN), Blacksburg, Virginia, USA*

† Electronic supplementary information (ESI) available: Photographic images of hydrogels obtained with different supplementations of CSL and GO; SEM morphology and TGA of membranes; size distribution of AuNPs obtained using DLS; calibration curves of AuNPs; membrane stability study under ultrasonication in solutions with different pH values; SEM, TGA and photothermal properties of GO. See DOI: https://doi.org/10.1039/d1en00754h

materials include Au and Ag nanostructures,[8] molybdenum disulfide,[9] titanium oxides,[10,11] and MXenes.[12] Similarly, carbon-based materials including nanocarbon and polymeric materials such as carbon black,[13] graphene (GO) or reduced graphene oxide (rGO),[14] carbon nanotubes,[15] polydopamine,[16] and polypyrrole have been proposed.[17] Graphene is considered one of the most interesting and low-cost 2D materials as it possesses excellent electrical, optical, thermal, photothermal, and mechanical properties.[18] GO absorbs visible and near-infrared light across a broad electromagnetic spectrum.[2,19,20] Due to electron excitation and the relaxation of loosely bound $\pi$ electrons, the conversion of incident light into heat occurs efficiently.[2,19,20] Photothermally active graphene-based thin film membranes minimize biofouling and selectively transport ions/molecules, while graphene-based thick foams generate steam and harvest clean water *via* distillation.[2,14,21]

Graphene-based membranes have been shown to demonstrate high water permeability and precise sieving ability.[22] However, the stability and durability of free-standing graphene/GO laminates are compromised for large-scale application due to the damage that can occur during operation.[14,23] Several porous polymeric support materials such as polysulfone,[24] polyethersulfone,[25] poly(vinylidene fluoride),[26] and polyvinyl alcohol[27] are being explored to improve the water permeability as well as the chemical and mechanical stability of graphene/GO-based membranes. Similarly, the use of graphene-based foams for solar evaporation processes requires three-dimensional porous bilayered materials consisting of a photothermal layer supported by a more rigid thermal insulation layer.[3,21] The photothermal layer absorbs broad-spectrum light while creating a localized heating interface for conversion of light into heat,[28,29] whereas the low thermal conductivity insulation layer increases water transport to the evaporation surface and minimizes heat transfer to bulk water.[3,21] Inexpensive low thermal conductivity support materials are used as insulation layers for solar steam generation, including non-carbohydrate polymers (lignin made of monomers of monolignols, *p*-coumaryl alcohol, coniferyl alcohol, and sinapyl alcohol)[30] and carbohydrate polymer (cellulose containing glucose as the monosaccharide unit)[31] based materials such as cotton,[32] wood,[33,34] bamboo,[35] and bacterial nanocellulose (BNC).[21]

BNC is extremely promising for the development of engineered materials owing to its high surface area, microporous nature, tensile and mechanical strength, and its facile biosynthesis and low environmental footprint.[36–39] Biosynthesis of BNC by bacteria within the *Gluconacetobacter* genus is widely reported.[38] These bacteria produce extracellular cellulose nanofibers that intertwine to form a porous 3D network.[40,41] Typically, the anchoring of graphene/GO sheets onto supporting polymers such as cellulose is carried out through techniques that include vacuum deposition and layer by layer assembly.[42–44] Some researchers, however, have reported the synthesis of a GO embedded BNC membrane *via* external incorporation of GO onto pre-synthesized BNC by vacuum filtration.[42,43] Unfortunately, the long-term chemical and mechanical stabilities of these membranes are insufficient.[14] Promisingly, the *in situ* incorporation of GO sheets within BNC fiber networks during the growth of *Gluconacetobacter* has led to increased structural integrity and stability of the composite membrane.[45–47] The incorporation of GO sheets within entangled BNC fibers occurs following the initial adsorption of GO sheets and subsequent biosynthesis of the BNC fibers.[45–47] *In situ* biosynthesis of a spherical structured GO/BNC hydrogel was reported using a dynamic cultivation route.[48,49] Meanwhile membrane-like structures were obtained with a static cultivation method.[14,21] The microbial growth kinetics of *in situ* biosynthesis of a rGO/BNC hydrogel and the analysis of percolated network formation were detailed by Dhar *et al.*[50] Incorporation of GO/rGO nanosheets into the intergalleries of BC nanofibers occurred through hydrogen bonding interactions and the growth kinetics were controlled by the carbon substrate as well as oxygen at the air–medium interface.[50] Applications of GO embedded BNC-based photothermal membranes for efficient biofouling-controlled ultrafiltration and solar steam generation processes were recently reported by Jiang *et al.*[14,21]

Jiang *et al.* introduced[21] a two-step bilayer production of a GO embedded BNC hydrogel where a pristine BNC layer was grown by adding a nutrient medium on top of a previously prepared GO/BNC hydrogel. The present study was conducted to (i) demonstrate reproducible single-step production of bilayer membranes and (ii) evaluate the utility of these bilayer membranes for versatile applications including filtration, photothermal disinfection, and steam generation. We developed a simple and novel, single-step biosynthesis by altering the growth medium through supplementation of corn steep liquor (CSL) as a growth enhancer. The influence of the composition of the growth medium (at different concentrations of growth substrate and GO mixtures) on the *in situ* formation of BNC and the subsequent incorporation of GO to the BNC fibers has not been previously evaluated. We hypothesized that (i) *in situ* integration of GO sheets within the growing BNC fiber matrix could be controlled by altering the growth rate of *Gluconacetobacter xylinus* and that (ii) bilayer formation of the hydrogel (GO embedded BNC layer and subsequent pristine BNC layer) in a single step occurs *via* control of two growth rate-based stages that occur during the incubation period. The following assessments were performed: (i) to evaluate the role of CSL as a growth enhancer for BNC growth rate modification, (ii) to reveal the growth rate controlled attachment of GO to the BNC fibers, (iii) to optimize the CSL supplement and GO loading in the growth medium to obtain a bilayer structured hydrogel with the desired biomass, (iv) to assess the filtration performance for the desired flux and particle rejection, (v) to study the photothermal inactivation of entrapped bacteria, and (vi) to evaluate water evaporation from the bilayer membrane.

 

# 2. Materials and methods

## 2.1. Materials

GO (0.4 wt%, monolayer content >95%) was purchased from MSE Supplies (Tucson, USA). Fructose (>99%), yeast extract, corn steep liquor (CSL), magnesium sulfate ($MgSO_4$, ≥99.5%), potassium dihydrogen phosphate ($KH_2PO_4$, 99.995%), sodium hydroxide (NaOH, ≥97.0%), and hydrochloric acid (HCl, 37%) were procured from Sigma-Aldrich, USA. All experiments were carried out using deionized water with a resistance ≥18 MΩ cm.

## 2.2. Production of bilayered rGO embedded BNC membranes

*G. xylinus* (ATCC® 10245™) was employed to produce bacterial nanocellulose fibers. A dense suspension of *G. xylinus* was cultured using a growth medium composed of 40 g fructose, 5 g yeast extract, 0.25 g $MgSO_4$, and 1 g $KH_2PO_4$ dissolved in 1 L deionized water. Dense bacterial cultures were obtained by inoculating 1 mL of *G. xylinus* (~$10^5$ CFU $mL^{-1}$) in 100 mL of growth medium and then incubating at 37 °C for 3 days at 150 rpm in a shaker incubator. During incubation, nascent BNC pellicles were developed at the air–liquid interface. At the conclusion of the incubation period, the cultured flask along with the BNC pellicle was vigorously shaken using a vortex shaker at 3200 rpm for 5 min to detach the bacteria from the BNC pellicle into the liquid medium. This suspension was used as pre-culture (~$10^8$–$10^9$ CFU $mL^{-1}$) in further experiments.

To study the influence of the CSL bacterial growth enhancer on the production of bilayered hydrogels, the growth medium was modified by addition of varying concentrations of CSL (0, 20, 40, 60, 80 mL of CSL per L of growth medium) to a fixed GO concentration of 0.05 w/v%. The modified growth media were inoculated with pre-cultured *G. xylinus* at 0.1 v/v%. The prepared mixtures, with a volume of 20 mL, were poured into disposable Petri dishes (100 mm diameter, 15 mm deep) and incubated at 37 °C for 72 h under aerobic and static conditions. To further optimize the GO loading onto the bilayered hydrogel, the growth media were modified with varied concentrations of GO (0.025, 0.05, 0.075 wt/v%) at a fixed CSL supplementation of 20 mL $L^{-1}$ and 0.1 v/v% of pre-culture. The GO embedded BNC hydrogels were boiled with 0.2 M NaOH for 1 h to eliminate attached bacteria and residual nutrient media. This process is known to result in the partial reduction of GO.[14] Cleaned hydrogels were then washed with deionized water for 48 h with periodic change of water. The purified hydrogels were freeze-dried for 24 h to acquire single-layered (rGO/BNC) and bilayered (rGO/BNC:BNC) membranes. Changes in the production of GO/BNC for different CSL and GO supplementations are listed in Table 1.

Table 1 Summary of single-layered (rGO/BNC) and bilayered (rGO/BNC:BNC) membranes produced in different growth media

| Membrane ID | CSL (mL $L^{-1}$) | GO loading (wt/v%) | Weight of hydrogel (g) | Dry weight (g) |
|---|---|---|---|---|
| M0 | 0 | 0.05 | 7.43 ± 0.68 | 0.022 ± 0.0019 |
| M1/G2 | 20 | 0.05 | 12.73 ± 0.14 | 0.057 ± 0.0047 |
| M2 | 40 | 0.05 | 13.28 ± 0.53 | 0.083 ± 0.0070 |
| M3 | 60 | 0.05 | 15.31 ± 0.58 | 0.108 ± 0.0043 |
| M4 | 80 | 0.05 | 17.87 ± 0.66 | 0.133 ± 0.0013 |
| G0 | 20 | 0 | 14.05 ± 0.71 | 0.091 ± 0.0022 |
| G1 | 20 | 0.025 | 11.36 ± 0.25 | 0.06 ± 0.0049 |
| G3 | 20 | 0.075 | 13.11 ± 0.47 | 0.07 ± 0.0018 |

## 2.3. Membrane characterization

Surface morphology and cross-sectional analyses of the membranes were performed using a Quanta 600 FEG environmental SEM with an operating voltage of 3 kV. Nonconductive BNC samples were sputter-coated with iridium before the analysis, while the conductive rGO/BNC membranes were directly analyzed without sputter coating. GO dispersion in ethanol (0.04 mg $mL^{-1}$) was drop-cast on a Si substrate for the SEM analysis. The chemical nature of the GO/rGO within the BNC membrane was probed using X-ray photoelectron spectroscopy (XPS). XPS spectra were collected using a PHI Quantera SXM (ULVAC-PHI, Japan) with a hemispherical energy analyzer and a monochromatic aluminum target. Survey spectra were collected at 25 W/15 kV with a spot size of 100 μm, 45° take-off angle, and 280 eV pass energy. A 69 eV pass energy with a 0.125 eV scan step was chosen for high resolution spectrum acquisition. To quantify the extent of GO anchoring to BNC, thermogravimetric analysis (TGA) was performed over the temperature range of 25–700 °C using a TA instrument TGA5500 with a heating rate of 10 °C $min^{-1}$ under a nitrogen atmosphere. Raman analysis of the GO was performed using a WITec Alpha 500R Raman spectrometer (785 nm laser; WITec GmbH, Ulm, Germany). The bilayer structure of the membrane was analyzed through digital photography using the 100× Olympus objective lens of the Raman microscope.

## 2.4. Filtration

The membrane filtration performance was determined using gold nanoparticles (AuNPs synthesized *via* citrate reduction;[51] average diameters of ≈4.2 nm (44.8 nmol $L^{-1}$) and ≈20.6 nm (1.93 nmol $L^{-1}$)) as well as plasmid DNA (70 ng $mL^{-1}$). A dead-end filtration set-up was used for the filtration experiments (8200 ultrafiltration stirred cell, Millipore Corporation) as explained by Riquelme Breazeal *et al.*[52] The suspensions of AuNPs with volumes of 10–25 mL were loaded into the stirred cell. All filtration experiments were carried out with an applied pressure of 30 psi; the pressure was built up and controlled through the supply of nitrogen gas with a pressure regulator. The permeate water flux was estimated based on the volume of the filtrate collected per unit area of the membrane per unit time. The as-synthesized AuNPs and their removal efficiency by filtration were analyzed using a Cary 5000 UV-vis-NIR spectrophotometer. To quantify plasmid DNA filtration, overnight *Escherichia coli* cultures of

100 mL (inoculated with 1 mL of ~$10^6$ CFU $mL^{-1}$) were used for the extraction of double-stranded (ds) plasmid DNA which was extracted using an E.Z.N.A. plasmid DNA Maxi kit (D6922-02). The DNA concentration was analyzed using a Qubit 2.0 fluorometer (Invitrogen, Thermo Fisher Scientific) and a Qubit dsDNA HS assay kit. The particle size of the AuNPs and the hydrodynamic diameter of the ds plasmid DNA were analyzed using dynamic light scattering (DLS) with a Nano ZS instrument (Malvern Corporation, Malvern, UK).

### 2.5. Photothermal disinfection

Filtration followed by photothermal disinfection of *E. coli* bacteria was studied. An *E. coli* suspension grown in LB broth was centrifuged at 3260 × *g* (Thermo Scientific Sorvall ST 8 centrifuge) to remove the residual medium and then rinsed twice with 1× phosphate-buffered saline (PBS). *E. coli* cells (~2.0 × $10^7$ CFU $mL^{-1}$) were suspended in PBS and used in filtration/photothermal disinfection studies. An *E. coli* suspension of 10 mL was filtered through the membranes to estimate their filtration efficiency. The collected filtrate was plated onto an LB agar medium *via* spread plating and then observed for bacterial colony formation for 24 h. Based on the estimated CFU $mL^{-1}$, the filtration efficiency was calculated. Membranes with attached *E. coli* were subsequently exposed to a solar simulator (Abet Technologies' Model 11002 SunLite, Connecticut, USA) with an intensity of 0.6 kW $m^{-2}$ (one sun) and an exposure area of 50 × 50 $cm^2$. The thermal profile of the exposed membrane was observed using a 320 × 240 infrared thermal imaging camera (Model HTI-19 with 300 000 pixels). Bacteria from the membrane before and after solar irradiation were collected by swabbing an inoculation loop across the surface. Subsequently, the inoculation loops were streaked onto agar plated with LB medium and the inoculated plates were incubated for 24 h to determine the photothermal disinfection ability.

### 2.6. Solar steam generation

A bilayered rGO/BNC:BNC membrane with a diameter and thickness of 5.1 cm and 1 mm, respectively, was floated on the top of a glass beaker (5.3 cm diameter, 7.5 cm height and 2 mm thickness) filled with deionized water. It was irradiated using a solar simulator with an intensity of 0.6 kW $m^{-2}$ (one sun) for 60 min. The thermal profile was then monitored using an IR camera. Steam generation experiments were carried out using deionized water. The water evaporation rate was evaluated by quantifying the weight loss of water per unit time per unit exposure area. The difference in weight was assessed through an electronic weighing balance, having an accuracy of 0.01 g.

## 3. Results and discussion

### 3.1. Biosynthesis of bilayered hydrogels

BNC biosynthesis occurs *via* two stages: (i) fast aerobic growth in the presence of excess carbon substrate and oxygen; (ii) static growth following depletion of carbon and oxygen.[16,21] In the absence of GO, the resulting BNC was white, translucent, and flexible. BNC formation begins at the air–liquid interface since it requires both oxygen and a carbon source. Once the entangled layer of cellulose fibers starts to develop at the surface, growth continues 'layer by layer'[14,21] with growth of subsequent layers occurring in the depth of the growth medium as oxygen diffuses inwardly. This process results in the formation of a network of dense, 3D structured, parallel-oriented entangled layers of BNC. When GO is included within the growth medium, BNC grows around the GO sheets leading to GO entanglement within the composite hydrogel. Adsorption of GO onto the slowly growing BNC layers ensured the formation of a compact GO/BNC composite hydrogel (*i.e.*, single-layered GO/BNC).[47] GO/BNC hydrogels were synthesized by growing *G. xylinus* in mixtures of nutrient medium modified with CSL and GO. To quantify how CSL influences the formation of the GO/BNC hydrogel, the bacterial growth medium was modified with varying amounts of CSL (0–80 mL CSL per L of standard nutrient medium) while maintaining the GO concentration at 0.05 wt%. The BNC biosynthesis rate is dependent upon the concentration of the CSL growth enhancer substrate. CSL is a viscous soluble product formed as a by-product of corn wet-milling. It is an excellent source of carbon and nitrogen as it contains various amino acids, vitamins, and minerals.[38] CSL addition to the growth medium enhances the *G. xylinus* growth and the production of BNC.[38,53,54] Modifications in the formation of bilayer structured GO embedded BNC hydrogels with varying quantities of supplemental CSL are shown in Fig. 1a. Photographic images presenting front and back views with varying levels of incorporation of GO within the BNC fibers depending on the CSL level are given in Fig. 1b. As expected, in the absence of CSL, the BNC growth rate was quite low. When CSL was added to the growth medium at ratios of 20–40 mL $L^{-1}$, the embedment of GO within the hydrogel resulted in production of two distinct layers: 1) a pristine BNC layer and 2) an adherent GO/BNC composite layer (*i.e.*, bilayered GO/BNC:BNC) (Fig. 1c and e). Because the growth of *G. xylinus* is enhanced by CSL, it is possible to produce a BNC layer at a rate that does not allow incorporation of GO during the initial incubation stage. As incubation proceeds, depletion of the CSL occurs simultaneous to a decrease in oxygen availability within the depth of the nutrient medium. This process reduces the BNC production rate; hence GO has the opportunity to adsorb onto the growing surface. As *G. xylinus* grows around the GO adsorbed BNC, a GO embedded BNC layer develops resulting in formation of the bilayered hydrogel. When the CSL concentration exceeded 40 mL $L^{-1}$, bilayer formation was not observed. The BNC formed under these conditions was similar to the pristine BNC since there was minimal observed attachment of GO. Under these conditions, GO weakly adsorbed onto the surface of BNC within the incubation period of 72 h, thus resulting in the formation of either a poorly embedded GO/BNC layer or a pristine BNC layer. Photographic images showing the minimal attachment of GO

 

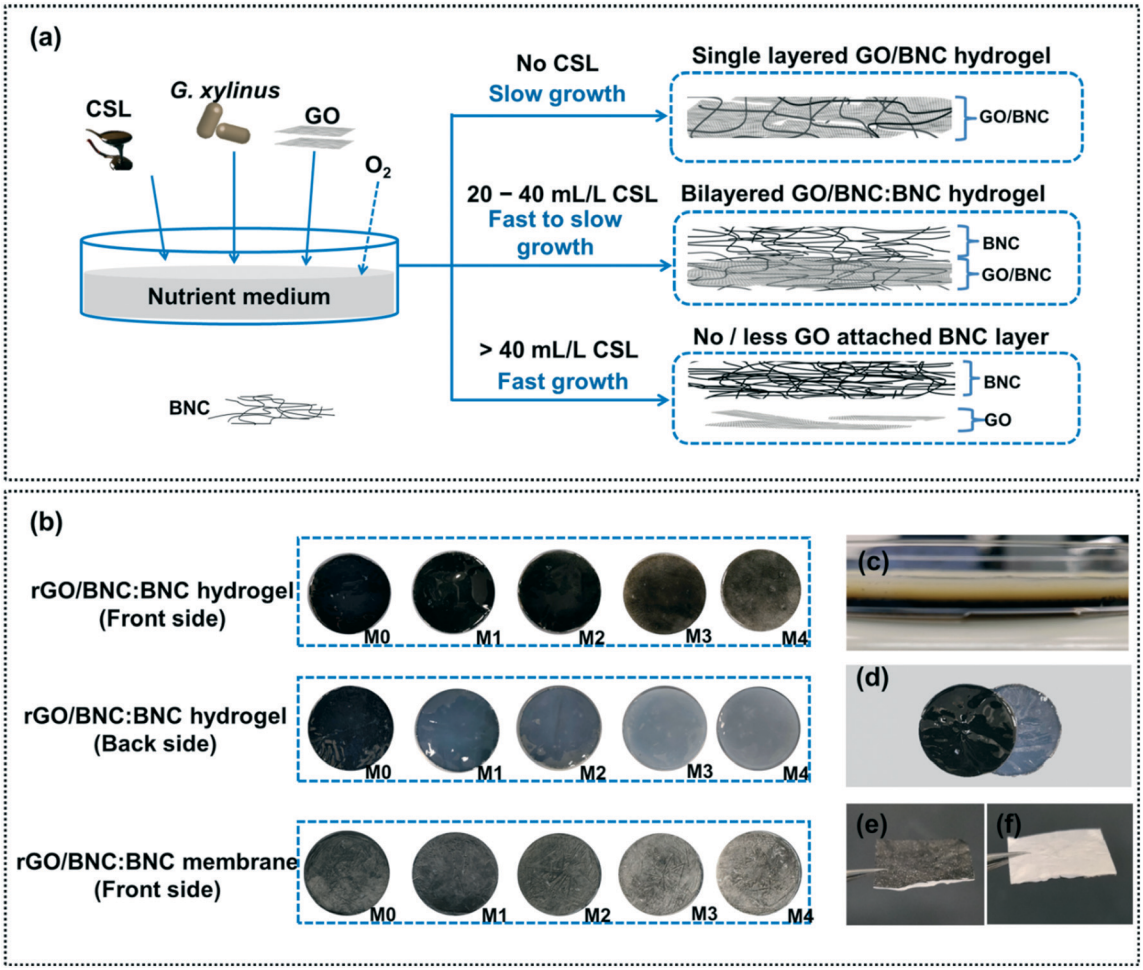


**Fig. 1** (a) Schematic illustration representing the influence of CSL on the biosynthesis of GO/BNC and GO/BNC:BNC hydrogels, (b) photographic images of rGO/BNC:BNC hydrogels (front and back surfaces) and membranes (front surface) representing the variation in the embedding of GO onto the entangled BNC fibers, photographic image of (c) uncleaned GO/BNC:BNC hydrogels presenting the intersection, (d) cleaned rGO/BNC:BNC hydrogels, and (e) and (f) the rGO/BNC:BNC membrane (front and back surface).

to the BNC fibers for CSL >80 mL $L^{-1}$ are shown in Fig. S1.† A sufficient quantity of GO is required to obtain perfectly stacked layers along with BNC fibers to achieve the final desired membrane pore size, particle rejection, and water flux. The addition of GO to the growth medium was varied as 0.025, 0.05, and 0.075 wt% to a fixed volume of growth medium. As shown in the ESI† (Fig. S2), 0.05 and 0.075 wt% loadings of GO were found to be sufficient to fully cover the BNC layers, whereas 0.025 wt% was insufficient.

### 3.2. Membrane characterization

SEM analysis was performed to characterize rGO incorporation into the entangled BNC fibers as a function of varying concentrations of CSL and GO. Pristine BNC has a porous 3D structure composed of entangled nonwoven nanofibrils having cross-sectional diameters of >100 nm (Fig. 2a). The addition of GO in the absence of CSL resulted in production of a freeze-dried rGO/BNC membrane (M0) consisting of loosely packed rGO anchored BNC fibers within a 3D porous network (Fig. S3a†). Cross-sectional SEM analysis of the M0 membrane shows that GO on BNC is anchored in a layered manner with a total thickness of ~200 μm (Fig. S2b†). The rGO/BNC:BNC bilayered membrane (M1) synthesized in the presence of 20 mL $L^{-1}$ CSL exhibited smooth, tightly packed, uniformly distributed rGO sheets anchored to the BNC nanofibrils (Fig. 2b and c). The cross-sectional confocal microscopy images of the M1 membrane show a bilayered structure consisting of rGO/BNC as one layer followed by a pristine BNC layer with a total membrane thickness of ~1 mm (Fig. 2d). The bilayered membrane (M2) formed with 40 mL $L^{-1}$ CSL exhibits a network of heterogeneously intact rGO embedded within the BNC composite (Fig. S3c†). The surface morphology of the M3 membrane developed in growth medium amended with 60 mL $L^{-1}$ CSL showed randomly anchored rGO flakes on the surface fibrils of the BNC layers. The fast-growing nature of the growth medium reduces the attachment of GO flakes to the BNC fibers (Fig. S3d†).

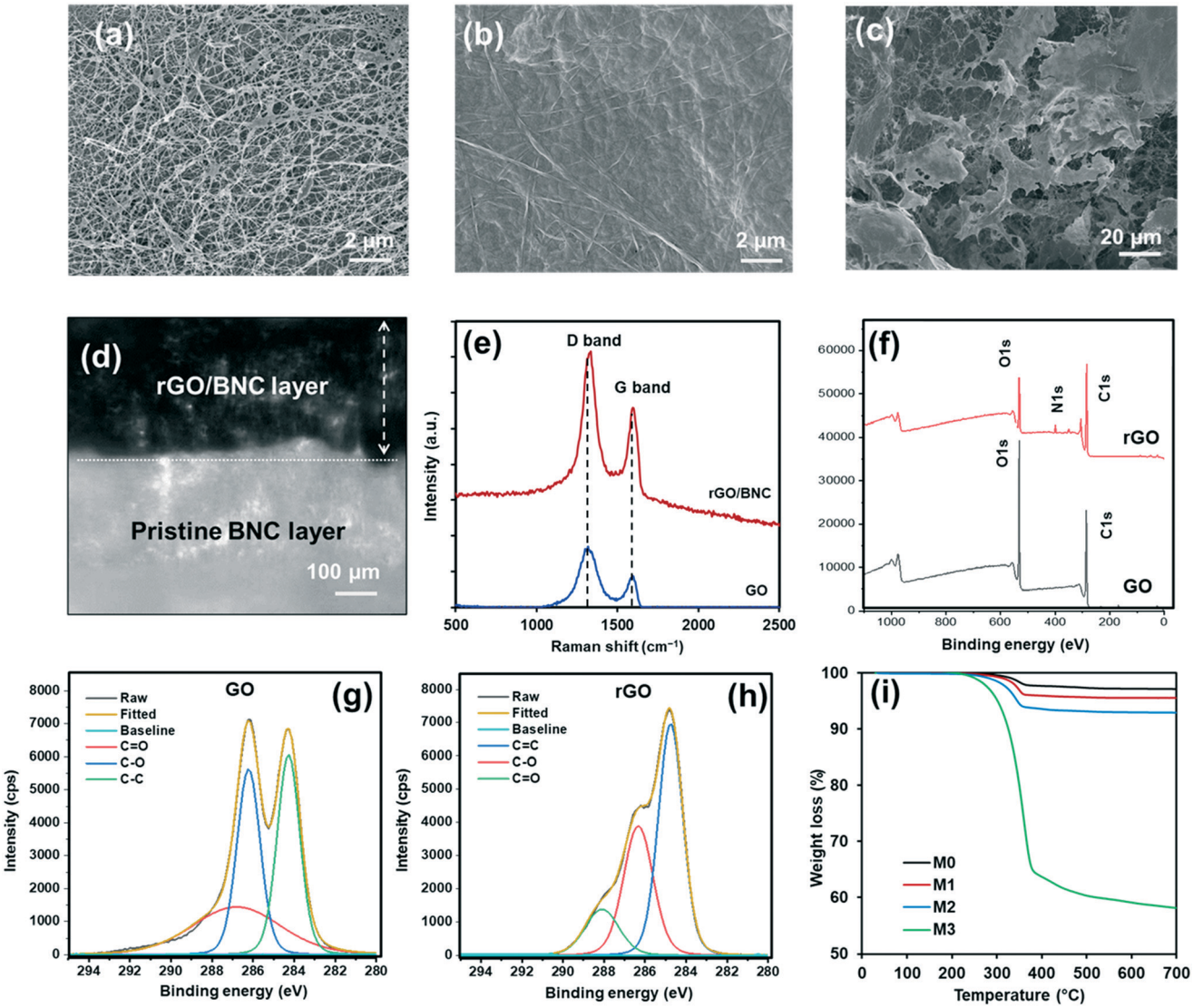


**Fig. 2** SEM surface morphology of (a) BNC, (b) the rGO/BNC:BNC membrane (low magnification) and (c) the rGO/BNC:BNC membrane (high magnification), (d) cross section image of the bilayer rGO/BNC:BNC membrane, (e) Raman spectra of GO and rGO/BNC (M1), (f) XPS survey scans of pristine GO and the rGO/BNC:BNC membrane, (g) C 1s high resolution spectrum of GO, (h) C 1s high resolution spectrum of rGO, and (i) TGA analysis of membranes M0–M3.

Raman analysis was performed to evaluate the quality of GO used in the hydrogels and rGO formed in the membranes. The typical characteristic features of the GO/rGO Raman spectrum are the graphite peak (G-band) and the defect peak (D-band; Fig. 2e). The G band of GO at 1596 $cm^{-1}$ results from $E_{2g}$ phonons at the Brillouin zone center corresponding to $sp^2$ carbon, while the D band at 1320 $cm^{-1}$ reflects defects in the graphene sheets corresponding to oxygen functional groups.[55] The intensity ratio of the D and G bands ($I_D/I_G$) was found to decrease from 2.86 (GO) to 1.67 (rGO/BNC). The higher $I_D/I_G$ of GO reflects defects introduced by the oxygen functional groups to the graphitic chains. The considerable recovery of the conjugated graphitic framework upon the de-functionalization of oxygen groups after sterilization and washing of the GO/BNC hydrogel under alkaline conditions resulted in the decreased $I_D/I_G$ of the rGO/BNC membrane. XPS analysis was carried out to further understand the extent of oxygen reduction during NaOH boiling. The survey spectra of GO and the cleaned/dried bilayer membrane show the reduction in the O1s signal following NaOH treatment (Fig. 2f). The high-resolution C 1s spectra of GO show binding energy configurations at 284 eV, 286.5 eV and 288.2 eV corresponding to $sp^2$ carbon (C═C) and oxidized $sp^3$ carbon representing the C═O and C–O functional groups[56,57] (Fig. 2g and h).

TGA analysis of the rGO/BNC (M0) and the rGO/BNC:BNC (M1–M3) bilayer membranes was done to understand the extent of attachment of the rGO sheets to BNC produced using different growth medium compositions (Fig. 2i). No significant weight loss was observed at temperatures <150 °C for all of the samples. Mass reductions of 2%, 4%, 6%, and 65% observed for the M0, M1, M2, and M3 membranes at

 

350 °C reflect the degradation of cellulose into $CO_2$ and $H_2O$. Additional reductions in weight were attributed to the decomposition of damaged graphitic carbon backbones and cellulose residues at temperatures >350 °C. Residual weights of 97% (M0), 96% (M1), 93% (M2), and 58% (M3) observed for the corresponding membranes indicate a pattern of increased weight loss for membranes as a function of the amount of BNC. A similar trend was observed for bilayered membranes produced with different loadings of rGO (G1–G3) (Fig. S4†). Bilayered membranes made with 0.025 wt% of GO showed 100% weight loss that could be attributed to the complete decomposition of the cellulose and the damaged graphitic carbon network. In the case of the G1 (0.05 wt% GO) and G2 (0.075 wt% GO) bilayered rGO/BNC:BNC membranes, residual weights of 97.8% and 93% were observed, respectively. The final weights represent the presence of a thermally stable graphitic carbon framework in the rGO of the rGO/BNC:BNC membrane that regained its properties during the boiling (cleaning step) of the GO/BNC:BNC hydrogel in NaOH.

Membrane stability was studied using ultrasonication under different pH conditions. Pieces of bilayered rGO/BNC:

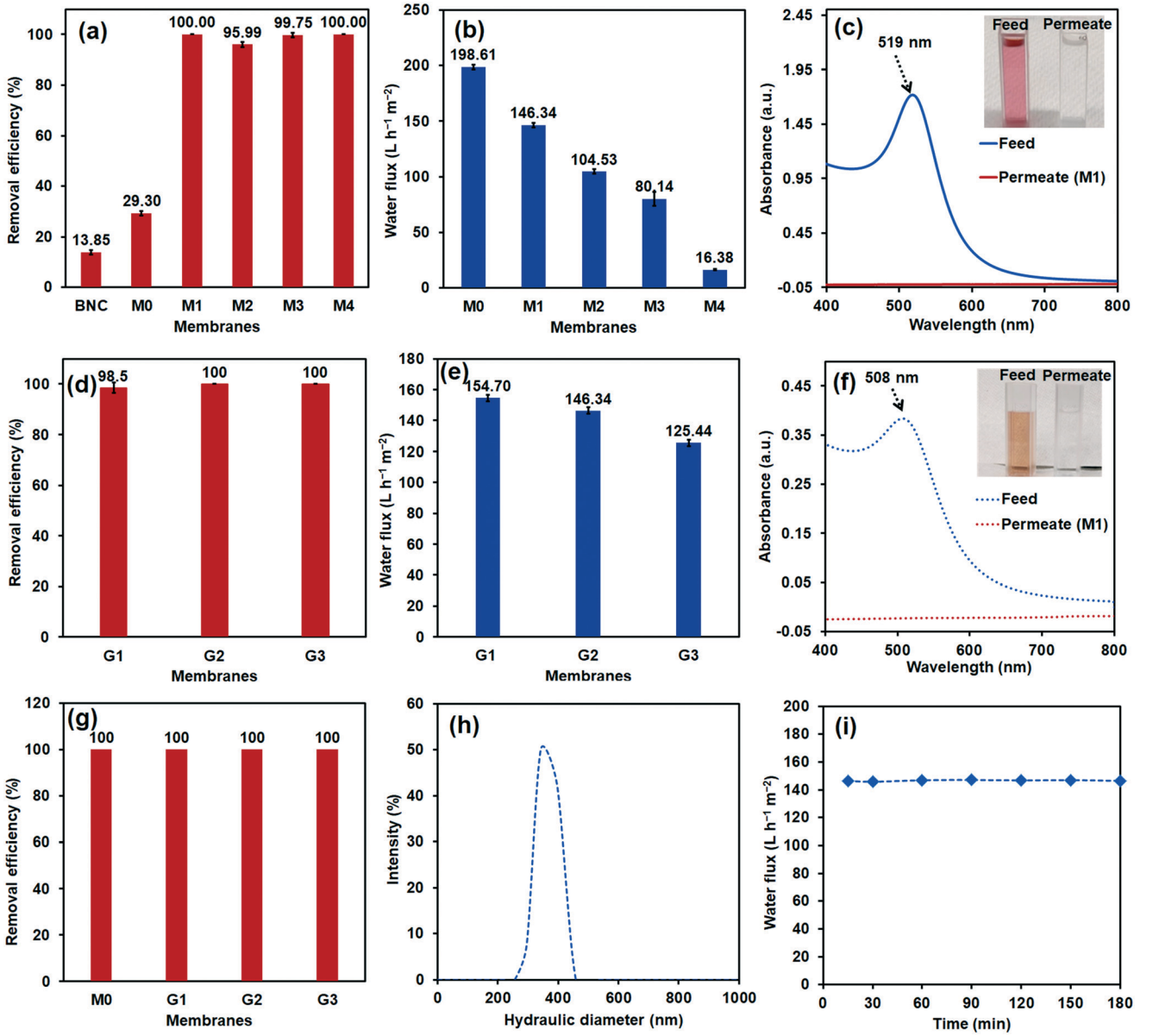


Fig. 3 (a) Removal efficiency of AuNPs (average diameter of 20.6 nm) at different membranes (BNC, M0–M4) in a dead-end filtration setup, (b) water fluxes of different membranes (BNC, M0–M4), (c) UV-vis spectra of AuNPs (average diameter of 20.6 nm) presenting the rejection efficiency in the M1 membrane, (d) removal efficiency of AuNPs (average diameter of 20.6 nm) at G1, G2 and G3 membranes, (e) water fluxes of G1, G2 and G3 membranes (BNC, M0–M4), (f) UV-vis spectra of AuNPs (average diameter of 4.2 nm) presenting the rejection efficiency in the M1 membrane, (g) filtration removal of ds plasmid DNA extracted from *E. coli*, (h) DLS analysis of ds plasmid DNA, and (i) variation in the water flux of the membrane (M1) over a run time of 180 min.

BNC membranes were soaked in glass beakers containing acidic (pH 2.1), neutral (pH 6.9) and alkaline solutions (pH 12.0) and ultra-sonicated for 3 h. The membranes were found to be intact and stable after sonication at all pH values (Fig. S7†).

### 3.3. Particle rejection and water flux studies

The particle rejection efficiency of the bilayered rGO/BNC:BNC membranes was tested using ≈21 nm AuNPs (Fig. 3a). The BNC membrane without rGO (G0) and the single-layered rGO/BNC membrane (M0) removed 13.9% and 29.3% of AuNPs, respectively. The M0 membrane composed of loosely packed rGO layers entangled within BNC did not provide pore sizes less than ~20.6 nm. Similarly, the low removal efficiency of AuNPs observed for the BNC membrane is a result of the fact that the entangled BNC contains an insufficient quantity of fibers to effectively remove the nanoparticles. The water flux of the M0 membrane was as high as 198.6 L $h^{-1}$ $m^{-2}$ and a water flux too high to be measured was observed for BNC mainly because of its large membrane pore size (Fig. 3b). In contrast, bilayered rGO/BNC:BNC membranes (M1 and M2) removed 100% and 96.0% of the AuNPs (~20.6 nm) and exhibited water fluxes of 146.3 and 104.5 L $h^{-1}$ $m^{-2}$, respectively. Fig. 3c presents the UV spectra of the AuNPs (~20.6 nm) before and after filtration. Based upon the comparison of the rejection rate and water flux of the membranes, membrane M1 was found to be the most efficient. This finding reflects that the optimal addition of CSL to the growth medium was 20 mL $L^{-1}$ followed by that for the M2 membrane (=40 mL $L^{-1}$ CSL). In the case of the M3 and M4 membranes, 99.8 and 100% removal values of AuNPs were observed. While improved rejection of AuNPs was observed for M3 and M4, they exhibited minimal water flux (73.2 L $h^{-1}$ $m^{-2}$ for M3 and 15.7 L $h^{-1}$ $m^{-2}$ for M4).

The M1 membrane was tested for the removal of smaller AuNPs (~4.2 nm) to quantify the effective pore size. Complete removal of AuNPs suggests that the rGO sheets were stacked along with the BNC in a manner that resulted in a final effective pore size of <4.2 nm (Fig. 3f). The water flux of M1 obtained at 30 psi pressure was comparable to that of a commercial ultrafiltration membrane (146.3 L $h^{-1}$ $m^{-2}$).[58] Although higher AuNP rejection was achieved with the M3 and M4 membranes, lower water fluxes were observed. The rejection of AuNPs and water fluxes were compared for the membranes produced with varying loads of GO (G1–G3). Complete removal of both 4.2 and 20.6 nm AuNPs by the G2 and G3 membranes with corresponding water fluxes of 146.3 and 123.5 L $h^{-1}$ $m^{-2}$ represents optimum performance. Meanwhile G1 removed 98.5% of 20 nm AuNPs with a water flux of 151.1 L $h^{-1}$ $m^{-2}$, suggesting that an insufficient amount of GO was entangled with BNC (Fig. 3d and e). The removal efficiency of plasmid DNA through different membranes was studied (G0, M1, M2, M3) (Fig. 3g). Complete removal (100%) of plasmid DNA was measured for all of the membranes since the size of the ds DNA was measured to be ~350 nm as per DLS analysis (Fig. 3h). Continuous monitoring of the membrane (M1) over 180 min of run time resulted in insignificant variation in the measured water flux (Fig. 3i).

### 3.4. Photothermal disinfection

To quantify the photothermal disinfection capacity of the membranes, *E. coli* stocks (~$2.0 \times 10^7$ CFU $mL^{-1}$) were filtered through the membranes and they were then exposed to solar irradiation for 10 min. The filtrate collected through the different membranes was analyzed to determine the removal efficiency of *E. coli* (Fig. 4a and b). All of the rGO embedded BNC membranes filtered the bacteria completely, whereas BNC alone showed a removal efficiency of 99.999%. The *E. coli* filtration efficiency is dependent on the membrane pore size and the rGO embedded BNC membranes (G0, G1, G2, G3) exhibit an appropriate pore size to exclude *E. coli* effectively. The ultrafiltration performance of these biosynthesized membranes is comparable to those of other non-biodegradable polymeric membranes in removing bacteria (Table S1†). It is evident that rGO has considerable photothermal properties under solar irradiation with the possibility of inactivating bacteria entrapped on and within the rGO/BNC:BNC membranes. The degree of photothermal disinfection is dependent on the magnitude of the local temperature rise and the duration of solar exposure.[33] The presence of abundant π electrons within the $sp^2$ carbon of rGO results in narrow energy levels, thus, exhibiting high light to heat conversion.[2,59] When solar light irradiated the surface, the surface temperature of the rGO embedded BNC membranes increased from 24 °C to 40–45 °C within 30 s of exposure (Fig. 4c) and reached 55–70 °C following 10 min of continuous exposure. Meanwhile the GO membrane reached up to 62 °C in 60 min of solar irradiation (Fig. S8c†). The rate of temperature increase for the BNC membrane was much less as it only reached 40 °C after 10 min. The temperature profile of the bilayer rGO/BNC:BNC membrane exhibited two stages.[60] In the first stage, the temperature plateaued within 10 and 25 min of exposure. During this stage, solar energy evaporated water molecules entrapped within the rGO/BNC medium. In the second stage, solar energy further raised the temperature until it attained equilibrium values of 83, 90.5, and 100 °C for bilayered membranes G1, G2, and G3, respectively. The rate of increase in temperature was dependent on the amount of rGO loaded on the BNC and follows the order: G3 > G2 > G1. The comparison of single layer rGO/BNC and bilayer rGO/BNC:BNC shows that the temperature change was more rapid for the single layer relative to the bilayer (Fig. 4d). However, there was no distinct two-stage temperature profile observed for the single layer rGO/BNC membrane. Due to the minimal water entrapping capacity of the single layer rGO/BNC membrane, solar energy is rapidly utilized to raise the temperature with a higher water evaporation rate. A

 

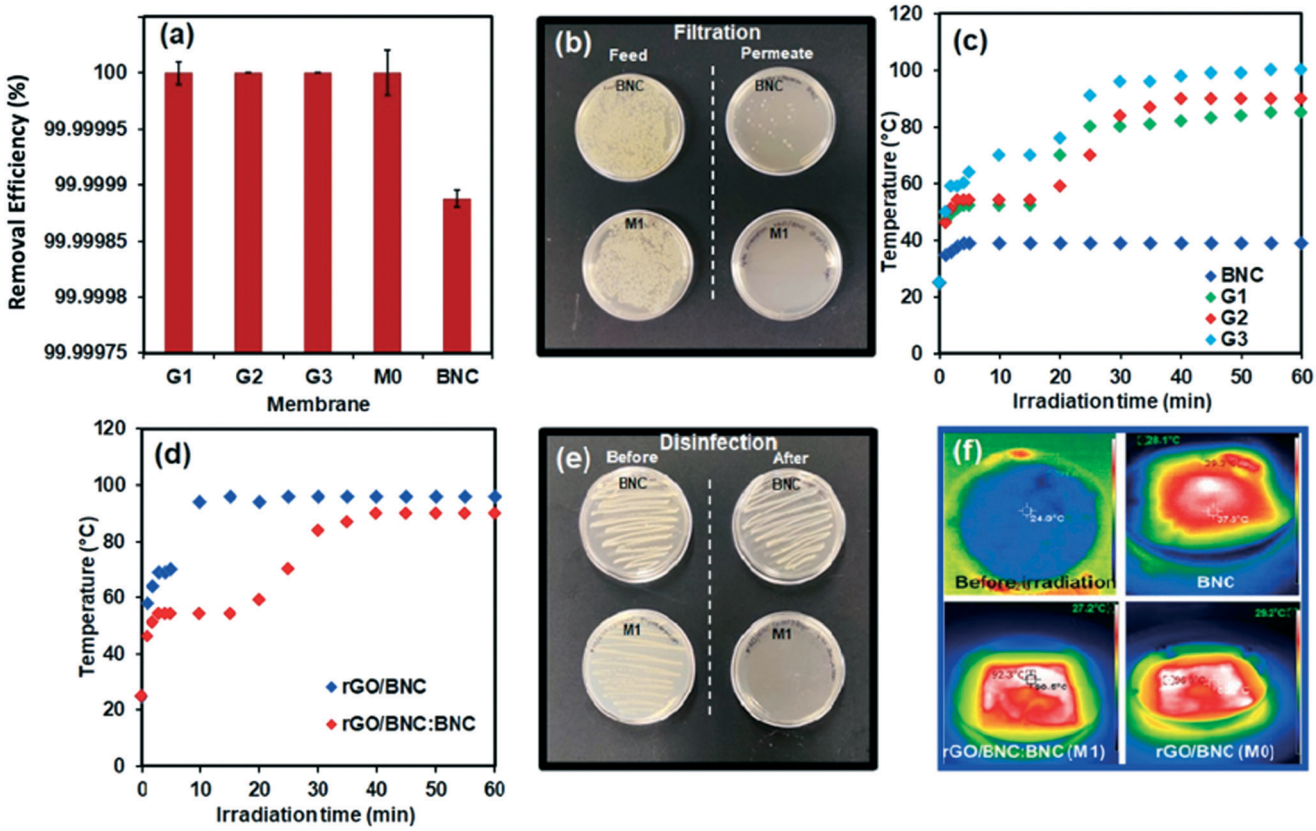


**Fig. 4** (a) Filtration removal of *E. coli* at different membranes (BNC, M0, G1–G3), (b) photographic images presenting the colony formation of the feed and permeate, (c) temperature profiles of rGO/BNC:BNC and BNC membranes and water during the solar irradiation, (d) temperature profiles of rGO/BNC (0.05 wt/v%) and rGO/BNC:BNC (0.05 wt/v%) during the solar irradiation, (e) bactericidal ability of photothermal membranes presented by the streak plating method and (f) IR images presenting the temperature variations of membranes (BNC, M0 and M1).

temperature range of 60–65 °C is sufficient to inactivate *E. coli* through the denaturation of cellular enzymes/proteins and cell membrane damage (Fig. 4e). Both single (0.05 wt% GO) and bilayer (0.05 and 0.075 wt% GO) rGO embedded BNC membranes inactivated *E. coli* cells completely (100% removal), while insignificant inactivation was observed with the BNC membrane. To understand the maximum rise in the temperatures of the membranes (BNC, M0 and M1), the irradiation was carried out for 60 min (Fig. 4f). The temperature of the BNC membrane reached only 39.3 °C while the M1 and M2 membranes achieved up to 92.3 and 96 °C, respectively. Control experiments in the absence of sunlight indicate that there is no biocidal effect imposed by the rGO/BNC membrane over a contact period of 60 min, and thus the measured inactivation solely reflects photothermal effects.

### 3.5. Solar steam generation

The capacity of the bilayer rGO/BNC:BNC membranes (0.05 wt% GO) and the rGO/BNC (0.05 wt% GO) and pristine BNC membranes to generate steam under simulated solar light was evaluated. Fig. 5a shows rapid water evaporation at the air/water interface upon floating of the bilayered membrane within the glass beaker. The steam generation efficiency of the membrane was determined based on the measured weight loss of water due to evaporation as a function of exposure area and irradiation time (Fig. 5b). The bilayer rGO/BNC:BNC membranes exhibited a water evaporation rate of 1.96 kg $m^{-2}$ $h^{-1}$ for the M1 membrane. In contrast, the BNC membrane alone and water without any membranes resulted in measured evaporation rates of only 0.6 and 0.47 kg $m^{-2}$ $h^{-1}$, respectively. The temperature of the M1 membrane reached 56.9 °C in 60 min whereas the water surface without the membrane reached only 32 °C (Fig. 5c). The bilayer membrane exhibited a 3.26 times greater evaporation rate than pristine BNC. The bilayer rGO/BNC:BNC membrane was reused 4 times, and constant evaporation rates were achieved without much variation, thus indicating that the membrane is highly stable and reusable. The water evaporation rate of the bilayer rGO/BNC: BNC (M1) membrane was 1.20 times higher than that of the rGO/BNC (M0) membrane (1.64 kg $m^{-2}$ $h^{-1}$). This value reflects the importance of the bilayered membrane to facilitate water evaporation. The presence of rGO in the rGO/BNC layer enhances absorption of incident light and photothermal conversion of absorbed light into heat. The properties of BNC such as its porous nature and hydrophobicity enable the rapid transport of water molecules

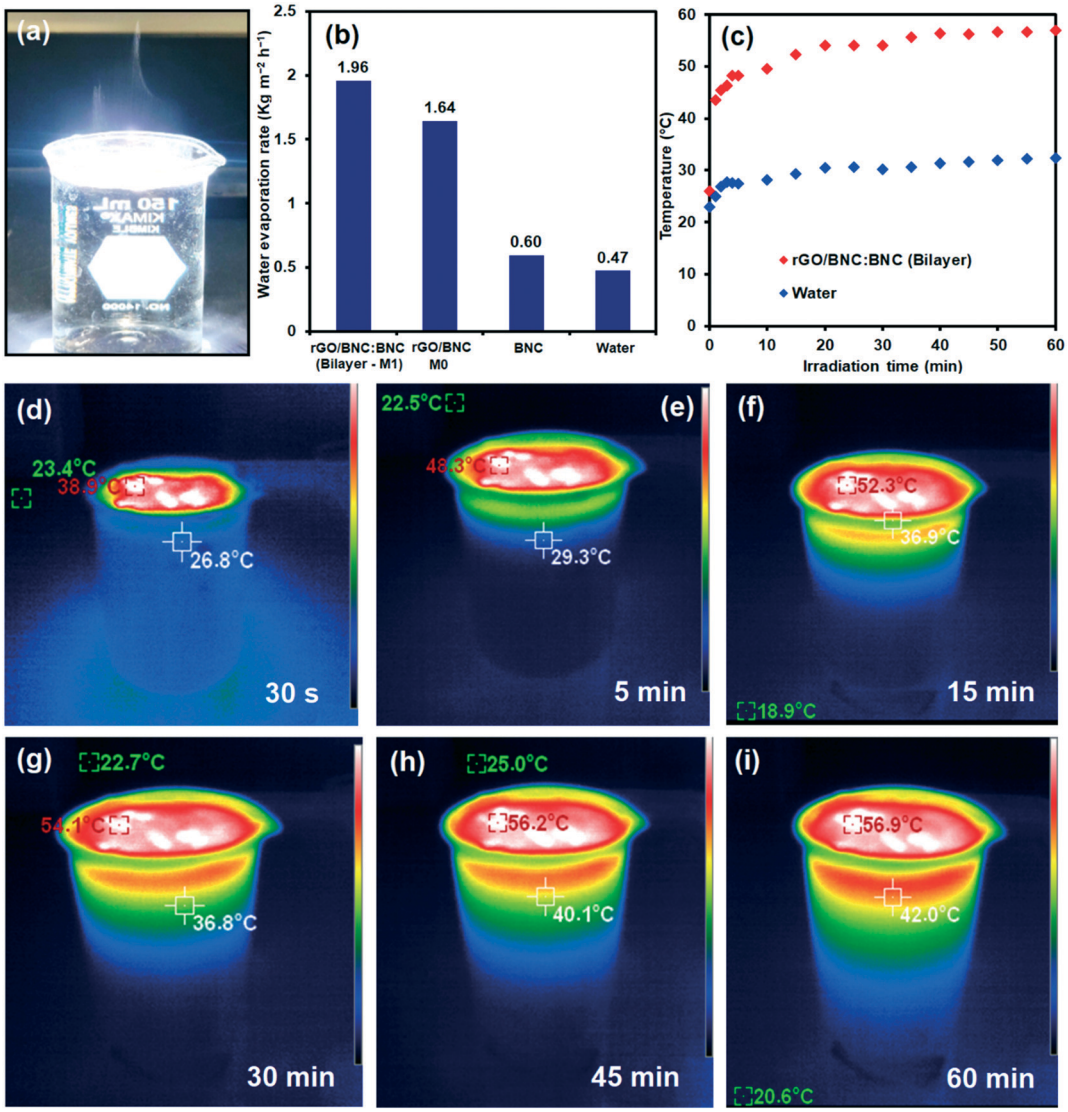


**Fig. 5** (a) Photographic image representing steam generation on bilayered rGO/BNC:BNC – M1 membrane, (b) water evaporation rates of BNC, rGO/BNC and rGO/BNC:BNC membranes, (c–i) IR camera images presenting the temperature changes at the air–liquid interface of the rGO/BNC:BNC membrane under solar irradiation with different time intervals.

from the bulk liquid phase to the evaporative membrane surface (*i.e.*, the light exposure layer of rGO/BNC).[61] The low thermal conductive property of the BNC could also prevent heat loss to the bulk liquid.[62]

The variation in temperature of the bilayered membrane (M1) floating at the air/liquid interface was captured using an IR camera. Upon solar light irradiation, the temperature rapidly increased to 38.9 °C from 25 °C within 30 s of exposure (Fig. 5d), while the temperature reached 48.3 °C after 5 min and 52.3 °C after 15 min (Fig. 5e and f). Due to the continuous exposure to simulated solar light, the surface temperature of the bilayered membrane reached 54 °C in 30 min and 56.2 °C in 45 min with a slow rate (Fig. 5g and h). A further change in temperature was not apparent and attained equilibrium upon extended exposure to irradiation. The rapid rise in the temperature is due to the combined properties of rGO and BNC. High absorption and manifold scattering of the incident light by rGO and BNC fibers respectively increase the optical path length and expand the absorption resulting in high heat conversion.[21,63] The performance of this biosynthesized photothermal foam towards steam generation is comparable to those of other GO/rGO-based polymeric membranes/foams (Table S2†).

## 4. Conclusions

This study illustrates the simple and novel one-step biosynthesis of a versatile bilayer GO embedded BNC hydrogel through an environmentally friendly approach. We found that the adsorption and incorporation of GO sheets onto the BNC fibers of the bilayered hydrogel can be controlled by varying the growth rates of the BNC and can be significantly

 

manipulated by supplementation of CSL growth enhancer compounds to the nutrient growth medium. The biosynthesis of the bilayer hydrogel occurs in two stages. In the initial stage of the hydrogel biosynthesis, the pristine BNC layer forms due to the fast growth rate and the minimal attachment of GO sheets. In the second stage, depletion of substrates (carbon and oxygen) reduce the growth rate of BNC, thus enhancing the adsorption and incorporation of GO into the BNC. The optimized moderate thickness of the bilayer rGO/BNC:BNC membrane allowed us to explore its versatile application for water purification, including particle filtration, photothermal disinfection of entrapped bacteria, and solar steam generation processes. The bilayered membrane exhibited high stability under variable mechanical and chemical environments and exhibited a high degree of reusability as indicated by water flux measurements (for M1: decreasing only from 145 to 130 L $h^{-1}$ $m^{-2}$ following filtration of *E. coli* and ultrasonic cleaning). This biobased membrane is more environmentally benign relative to synthetic and metal incorporated membranes. Moreover, the simple and non-toxic biosynthesis approach demonstrated in this study can also find utility for the production of a variety of functional nanocomposites containing alternative 2D materials. Such nanocomposites will be useful for applications in catalysis, sensors, drug delivery, energy harvesting and storage.

## Author contributions

G. Divyapriya directed the research effort, wrote the manuscript, and provided oversight of the research team. A. Rahman, W. Leng, and W. Wang provided the experimental results and aided in the writing of the manuscript. P. Vikesland obtained the research funding, provided oversight of the project, and collaborated in the writing and editing of the manuscript. All authors contributed to the development of the manuscript and its revision.

## Conflicts of interest

The authors declare no competing financial interest.

## Acknowledgements

This research was supported by the Fulbright Program, United States-India Educational Foundation, India, and Institute of International Education, USA (2471/FNPDR/2019) and NSF PIRE grant (1545756). Laboratory and instrumentation support was provided by the Virginia Tech Institute of Critical Technology and Applied Science (ICTAS) Sustainable Nanotechnology Center, Blacksburg, USA.

## References

1 Y. Lin, H. Xu, X. Shan, Y. Di, A. Zhao, Y. Hu and Z. Gan, *J. Mater. Chem. A*, 2019, **7**, 19203–19227.
2 Y. S. Jun, X. Wu, D. Ghim, Q. Jiang, S. Cao and S. Singamaneni, *Acc. Chem. Res.*, 2019, **52**, 1215–1225.
3 C. Zhang, H. Q. Liang, Z. K. Xu and Z. Wang, *Adv. Sci.*, 2019, **6**(18), 1900883.
4 X. Song, Y. Wang, C. Wang, M. Huang, S. Gul and H. Jiang, *ACS Sustainable Chem. Eng.*, 2019, **7**, 4889–4896.
5 L. Shi, Y. Shi, C. Zhang, S. Zhuo, W. Wang, R. Li and P. Wang, *Energy Technol.*, 2020, **2000456**, 1–10.
6 V. Nair, M. J. Muñoz-Batista, M. Fernández-García, R. Luque and J. C. Colmenares, *ChemSusChem*, 2019, **12**, 2098–2116.
7 D. Hao, Y. Yang, B. Xu and Z. Cai, *ACS Sustainable Chem. Eng.*, 2018, **6**, 10789–10797.
8 L. Noureen, Z. Xie, Y. Gao, M. Li, M. Hussain, K. Wang, L. Zhang and J. Zhu, *ACS Appl. Mater. Interfaces*, 2020, **12**, 6343–6350.
9 X. Yang, Y. Yang, L. Fu, M. Zou, Z. Li, A. Cao and Q. Yuan, *Adv. Funct. Mater.*, 2018, **28**, 1–9.
10 J. Wang, Y. Li, L. Deng, N. Wei, Y. Weng, S. Dong, D. Qi, J. Qiu, X. Chen and T. Wu, *Adv. Mater.*, 2017, **29**, 1–6.
11 Q. Wang, L. Qiu, Y. Jia, Y. Chang, X. Tan, L. Yang and H. Chen, *Sol. Energy Mater. Sol. Cells*, 2019, **202**, 110116.
12 X. J. Zha, X. Zhao, J. H. Pu, L. S. Tang, K. Ke, R. Y. Bao, L. Bai, Z. Y. Liu, M. B. Yang and W. Yang, *ACS Appl. Mater. Interfaces*, 2019, **11**, 36589–36597.
13 W. Xu, X. Hu, S. Zhuang, Y. Wang, X. Li, L. Zhou, S. Zhu and J. Zhu, *Adv. Energy Mater.*, 2018, **8**(14), 1702884.
14 Q. Jiang, D. Ghim, S. Cao, S. Tadepalli, K. K. Liu, H. Kwon, J. Luan, Y. Min, Y. S. Jun and S. Singamaneni, *Environ. Sci. Technol.*, 2019, **53**, 412–421.
15 Y. Wang, C. Wang, X. Song, S. K. Megarajan and H. Jiang, *J. Mater. Chem. A*, 2018, **6**, 963–971.
16 Q. Jiang, H. Gholami Derami, D. Ghim, S. Cao, Y. S. Jun and S. Singamaneni, *J. Mater. Chem. A*, 2017, **5**, 18397–18402.
17 Y. Wang, C. Wang, X. Song, M. Huang, S. K. Megarajan, S. F. Shaukat and H. Jiang, *J. Mater. Chem. A*, 2018, **6**, 9874–9881.
18 Z. Xie, Y. P. Peng, L. Yu, C. Xing, M. Qiu, J. Hu and H. Zhang, *Sol. RRL*, 2020, **4**, 1–28.
19 G. Liu, J. Xu and K. Wang, *Nano Energy*, 2017, **41**, 269–284.
20 P. Wang, *Environ. Sci.: Nano*, 2018, **5**, 1078–1089.
21 Q. Jiang, L. Tian, K. K. Liu, S. Tadepalli, R. Raliya, P. Biswas, R. R. Naik and S. Singamaneni, *Adv. Mater.*, 2016, **28**, 9400–9407.
22 F. Perreault, A. Fonseca De Faria and M. Elimelech, *Chem. Soc. Rev.*, 2015, **44**, 5861–5896.
23 C. N. Yeh, K. Raidongia, J. Shao, Q. H. Yang and J. Huang, *Nat. Chem.*, 2015, **7**, 166–170.
24 Y. Jiang, Q. Zeng, P. Biswas and J. D. Fortner, *J. Membr. Sci.*, 2019, **581**, 453–461.
25 M. Z. Fahmi, M. Wathoniyyah, M. Khasanah, Y. Rahardjo, S. Wafiroh and Abdulloh, *RSC Adv.*, 2018, **8**, 931–937.
26 F. Guo, C. Zhang, Q. Wang, W. Hu, J. Cao, J. Yao, L. Jiang and Z. Wu, *J. Appl. Polym. Sci.*, 2019, **136**, 28–30.
27 X. Zhou, F. Zhao, Y. Guo, Y. Zhang and G. Yu, *Energy Environ. Sci.*, 2018, **11**, 1985–1992.
28 Y. Wang, Z. Zhang, T. Li, P. Ma, H. Zhang, M. Chen, M. Du and W. Dong, *ACS Appl. Mater. Interfaces*, 2019, **11**, 44886–44893.

29 Z. Xie, Y. Duo, Z. Lin, T. Fan, C. Xing, L. Yu, R. Wang, M. Qiu, Y. Zhang, Y. Zhao, X. Yan and H. Zhang, *Adv. Sci.*, 2020, **7**(5), 1902236.
30 J. C. Del Río, J. Rencoret, A. Gutiérrez, T. Elder, H. Kim and J. Ralph, *ACS Sustainable Chem. Eng.*, 2020, **8**, 4997–5012.
31 S. Sun, S. Sun, X. Cao and R. Sun, *Bioresour. Technol.*, 2016, **199**, 49–58.
32 X. Wu, L. Wu, J. Tan, G. Y. Chen, G. Owens and H. Xu, *J. Mater. Chem. A*, 2018, **6**, 12267–12274.
33 K. Liu, Q. Jiang, S. Tadepalli, R. Raliya, P. Biswas, R. R. Naik and S. Singamaneni, *ACS Appl. Mater. Interfaces*, 2017, **9**, 7675–7681.
34 H. Liu, C. Chen, G. Chen, Y. Kuang, X. Zhao, J. Song, C. Jia, X. Xu, E. Hitz, H. Xie, S. Wang, F. Jiang, T. Li, Y. Li, A. Gong, R. Yang, S. Das and L. Hu, *Adv. Energy Mater.*, 2018, **8**(8), 1701616.
35 Z. Li, C. Wang, T. Lei, H. Ma, J. Su, S. Ling and W. Wang, *Adv. Sustainable Syst.*, 2019, **3**, 1800144.
36 H. Wei, K. Rodriguez, S. Renneckar, W. Leng and P. J. Vikesland, *Analyst*, 2015, **140**, 5640–5649.
37 S. Kang, A. Rahman, E. Boeding and P. J. Vikesland, *Analyst*, 2020, **145**, 4358–4368.
38 A. F. S. Costa, F. C. G. Almeida, G. M. Vinhas and L. A. Sarubbo, *Front. Microbiol.*, 2017, **8**, 1–12.
39 A. Sharma, M. Thakur, M. Bhattacharya, T. Mandal and S. Goswami, *Biotechnol. Rep.*, 2019, **21**, e00316.
40 A. F. Jozala, L. C. de Lencastre-Novaes, A. M. Lopes, V. de Carvalho Santos-Ebinuma, P. G. Mazzola, A. Pessoa-Jr, D. Grotto, M. Gerenutti and M. V. Chaud, *Appl. Microbiol. Biotechnol.*, 2016, **100**, 2063–2072.
41 H. Gao, Q. Sun, Z. Han, J. Li, B. Liao, L. Hu, J. Huang, C. Zou, C. Jia, J. Huang, Z. Chang, D. Jiang and M. Jin, *Carbohydr. Polym.*, 2020, **227**, 115323.
42 H. Luo, J. Dong, F. Yao, Z. Yang, W. Li, J. Wang, X. Xu, J. Hu and Y. Wan, *Nano-Micro Lett.*, 2018, **10**, 1–10.
43 Q. Fang, X. Zhou, W. Deng, Z. Zheng and Z. Liu, *Sci. Rep.*, 2016, **6**, 1–11.
44 P. Liu, C. Zhu and A. P. Mathew, *J. Hazard. Mater.*, 2019, **371**, 484–493.
45 P. Dhar, J. Etula and S. B. Bankar, *ACS Appl. Bio Mater.*, 2019, **2**, 4052–4066.
46 H. Si, H. Luo, G. Xiong, Z. Yang, S. R. Raman, R. Guo and Y. Wan, *Macromol. Rapid Commun.*, 2014, **35**, 1706–1711.
47 A. G. Nandgaonkar, Q. Wang, K. Fu, W. E. Krause, Q. Wei, R. Gorga and L. A. Lucia, *Green Chem.*, 2014, **16**, 3195–3201.
48 W. Zhu, W. Li, Y. He and T. Duan, *Appl. Surf. Sci.*, 2015, **338**, 22–26.
49 L. Urbina, A. Eceiza, N. Gabilondo, M. Á. Corcuera and A. Retegi, *Int. J. Biol. Macromol.*, 2020, **163**, 1249–1260.
50 P. Dhar, J. Etula and S. B. Bankar, *ACS Appl. Bio Mater.*, 2019, **2**, 4052–4066.
51 W. Leng, P. Pati and P. J. Vikesland, *Environ. Sci.: Nano*, 2015, **2**, 440–453.
52 M. V. Riquelme Breazeal, J. T. Novak, P. J. Vikesland and A. Pruden, *Water Res.*, 2013, **47**, 130–140.
53 P. Cerrutti, P. Roldán, R. M. García, M. A. Galvagno, A. Vázquez and M. L. Foresti, *J. Appl. Polym. Sci.*, 2016, **133**, 1–9.
54 H. E. Kennedy, M. L. Speck and L. W. Aurand, *J. Bacteriol.*, 1955, **70**, 70–77.
55 G. Divyapriya, R. Srinivasan, I. M. Nambi and J. Senthilnathan, *Electrochim. Acta*, 2018, **283**, 858–870.
56 G. Divyapriya, I. M. Nambi and J. Senthilnathan, *Chemosphere*, 2018, **209**, 113–123.
57 G. Divyapriya, I. M. Nambi and J. Senthilnathan, *Chem. Eng. J.*, 2017, **316**, 964–977.
58 R. Singh, in *Membrane Technology and Engineering for Water Purification*, 2015, pp. 1–80.
59 D. P. Storer, J. L. Phelps, X. Wu, G. Owens, N. I. Khan and H. Xu, *ACS Appl. Mater. Interfaces*, 2020, **12**, 15279–15287.
60 D. Li, Q. Zhao, S. Zhang, F. Wu, X. Yu, Z. Xiong, W. Ma, D. Wang, X. Zhang and B. Xing, *Environ. Sci.: Nano*, 2019, **6**, 2977–2985.
61 X. Li, G. Ni, T. Cooper, N. Xu, J. Li, L. Zhou, X. Hu, B. Zhu, P. Yao and J. Zhu, *Joule*, 2019, **3**, 1798–1803.
62 K. Uetani and K. Hatori, *Sci. Technol. Adv. Mater.*, 2017, **18**, 877–892.
63 Y. Yang, R. Zhao, T. Zhang, K. Zhao, P. Xiao, Y. Ma, P. M. Ajayan, G. Shi and Y. Chen, *ACS Nano*, 2018, **12**, 829–835.

 